Chaos, Solitons and Fractals 182 (2024) 114803

Contents lists available at ScienceDirect

Chaos, Solitons and Fractals

journal homepage: www.elsevier.com/locate/chaos

The Allen–Cahn model with a time-dependent parameter for motion by mean curvature up to the singularity

Junxiang Yang [a], Dongsun Lee [b], Soobin Kwak [c], Seokjun Ham [c], Junseok Kim [c,*]

[a] School of Computer Science and Engineering, Faculty of Innovation Engineering, Macau University of Science and Technology, Macao Special Administrative Region of China

[b] Department of Mathematics Education, Incheon National University, Incheon 21999, Republic of Korea

[c] Department of Mathematics, Korea University, Seoul, 02841, Republic of Korea

ARTICLE INFO

Keywords:
Modified Allen–Cahn equation
Singularity
Finite difference scheme

ABSTRACT

In this article, we investigate the temporal evolution of arbitrary, simple, closed two-dimensional (2D) and three-dimensional (3D) interfaces under motion driven by mean curvature up to a singularity. To facilitate this investigation, we propose a novel Allen–Cahn (AC) model with a time-dependent interfacial thickness parameter. The original AC equation was developed to model the phase separation of a binary mixture. It is well known that a level set or interface of the solution of the AC equation obeys the dynamics of motion by curvature as the interfacial thickness parameter approaches zero. Generally, it is difficult to find a closed-form analytic solution of the AC equation with any initial condition. Therefore, we need to estimate the solution of the AC equation through computational approaches such as finite difference method (FDM), finite element method (FEM), Fourier-spectral method (FSM), and finite volume method (FVM). Any simple, closed curves and convex surfaces eventually shrink to a point due to motion by mean curvature. Therefore, it becomes necessary to use adaptive mesh techniques to resolve this small size problem. However, even though we use adaptive mesh techniques, we still confront the relatively thick interfacial transition layer when the curves or interfaces become very small. To avoid this problem, we can start with a very small mesh size for a small value of the interfacial parameter, which results in an extremely high computational cost even when using adaptive mesh techniques. To resolve these issues, we present the AC equation with a time-dependent interfacial parameter and develop an adaptive mesh refinement system. To show the superior performance of the proposed mathematical equation and its computational algorithm, we present various numerical experiments and investigate the motion by mean curvature up to the singularity of curves in 2D space and interfaces in 3D space.

1. Introduction

We study the temporal evolution of arbitrary, simple, closed two-dimensional (2D) and three-dimensional (3D) convex interfaces under motion by mean curvature up to the singularity using the following Allen–Cahn (AC) model with a time-dependent interfacial thickness parameter:

$$\frac{\partial \phi}{\partial t} = -\frac{F'(\phi)}{\epsilon^2(t)} + \Delta\phi, \tag{1}$$

where $\Omega \subset \mathbb{R}^2$ or $\mathbb{R}^3$ is a domain. Here, the phase-field $\phi(\mathbf{x}, t)$ is a phase field, $F(\phi) = (\phi^2 - 1)^2/4$, and $\epsilon(t)$ is the time-dependent parameter related to the thickness of the interfacial transition layer. For simplicity, we use the negative one Dirichlet boundary condition, i.e., $\phi(\mathbf{x}, t) = -1$ for $\mathbf{x} \in \partial\Omega$.

If $\epsilon(t) = \epsilon$ is a time-independent constant in the proposed novel AC equation (1), then it becomes the original AC equation [1], which was proposed to model the phase separation of a binary mixture. It is well recognized that as ϵ approaches zero, the level set or interface of ϕ converges to motion by mean curvature at the boundary between phases, see [2–5] and references therein. Generally, it is difficult to find a closed-form solution of the AC equation with an arbitrary shaped initial interface except for some special initial conditions and domains. Therefore, we need to approximate the solution of the AC equation using numerical methods such as the finite difference method

* Corresponding author.
E-mail address: cfdkim@korea.ac.kr (J. Kim).
URL: https://mathematicians.korea.ac.kr/cfdkim (J. Kim).

https://doi.org/10.1016/j.chaos.2024.114803
Received 18 December 2023; Received in revised form 9 March 2024; Accepted 24 March 2024
Available online 27 March 2024

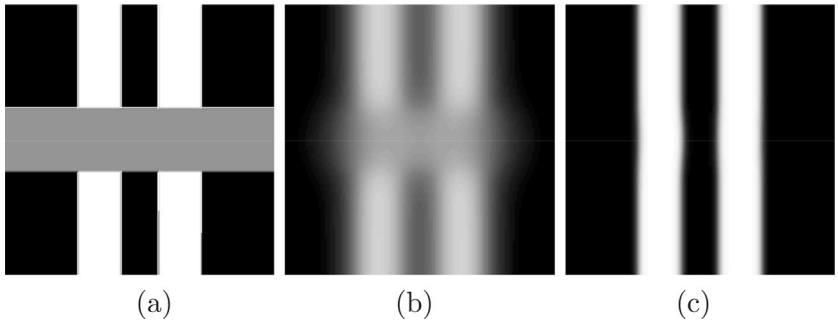

Fig. 1. Example of using a two-scale parameter: (a) the initial condition with a gray inpainting region, (b) the result after 50 temporal iterations with $\epsilon = 0.8$, and (c) the result after 700 temporal iterations with $\epsilon = 0.01$.
Source: Reprinted from Jeong et al. [20] with permission from J. KSIAM.

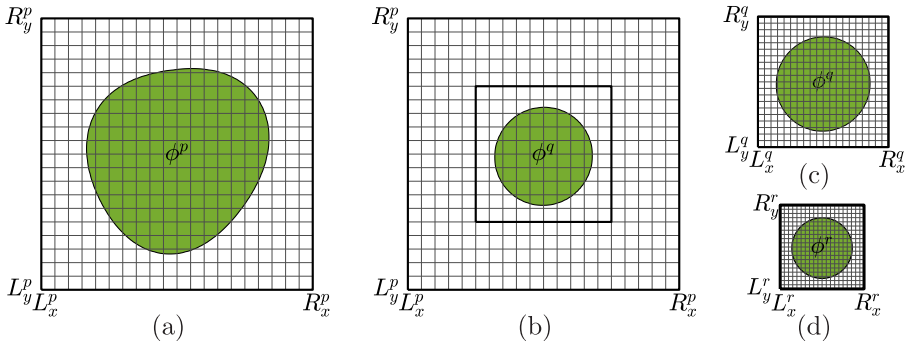

Fig. 2. Schematic illustration of the adaptive mesh refinement for discrete domains.

(FDM) [6–9], Fourier spectral method (FSM) [10–12], finite volume method (FVM) [13], and finite element method (FEM) [14–16].

Over time, any simple, closed curves and convex surfaces gradually diminish in size and eventually shrink to a single point due to motion by mean curvature [17]. Hence, the utilization of adaptive mesh strategies becomes imperative to address the issue of diminishing sizes. However, even with the application of these adaptive mesh techniques, we encounter a relatively thick interfacial transition layer as the curves or interfaces reach exceedingly small sizes. To circumvent this issue, one approach is to initiate the process with an exceedingly fine mesh size for a small interfacial parameter value. Nevertheless, this choice leads to an exceptionally steep increase in computational expenses, even when employing adaptive mesh techniques and parallel computing. To resolve these problems, we propose the above-mentioned AC equation with a time-dependent interfacial parameter, Eq. (1) and develop an adaptive mesh refinement algorithm. To validate the superior performance of the proposed novel modified AC equation and its numerical approach, we conduct various computational tests involving the investigation of curvature-driven motion right up to the point where curves and interfaces reach singularities.

It is worth noting that prior research has explored changing model parameter studies during simulations of image inpainting problems [18]. Fig. 1 shows the inpainting of a double stripe using Bertozzi's scheme [18] based on the following phase-field model derived from the Cahn–Hilliard equation [19]:

$$\frac{\partial c(\mathbf{x},t)}{\partial t} = \Delta[F'(c(\mathbf{x},t)) - \epsilon^2 \Delta c(\mathbf{x},t)] + \lambda(\mathbf{x})(f(\mathbf{x}) - c(\mathbf{x},t)), \tag{2}$$

where $F(c) = 0.25c^2(1-c)^2$, $f(\mathbf{x})$ a given image, and $\lambda(\mathbf{x})$ is a fidelity parameter.

Fig. 1(a), (b), and (c) display the initial condition with a gray inpainting region, the result after 50 temporal iterations with $\epsilon = 0.8$, and the result after 700 temporal iterations with $\epsilon = 0.01$, respectively. The computations were initiated using a relatively large $\epsilon = 0.8$ value and then changed to a smaller $\epsilon = 0.01$ value after completing 50 iterations. However, in the above-mentioned research, the model parameters were changed only once, and there was no refinement in grid resolution. The authors in [21] presented a mathematical model with space-dependent parameters to simulate nonhomogeneous zebra pattern formation.

The primary purpose of this study is to propose the AC equation with a time-dependent interfacial parameter and develop an adaptive mesh refinement system. As we reduce the numerical mesh size, we concurrently decrease $\epsilon(t)$.

The organization of this paper is as follows. In Sections 2 and 3, we present the 2D and 3D numerical solution algorithms and various computational tests, such as motion by mean curvature flows up to the singularity of interfaces to validate the superior performance of the proposed novel AC model with a time-dependent interfacial parameter and its efficient numerical algorithm. Finally, in Section 4, conclusions are drawn.

2. Two-dimensional space

Now, we present a computational algorithm and perform numerical experiments for the 2D AC equation with a time-dependent parameter for motion by mean curvature up to the singularity.

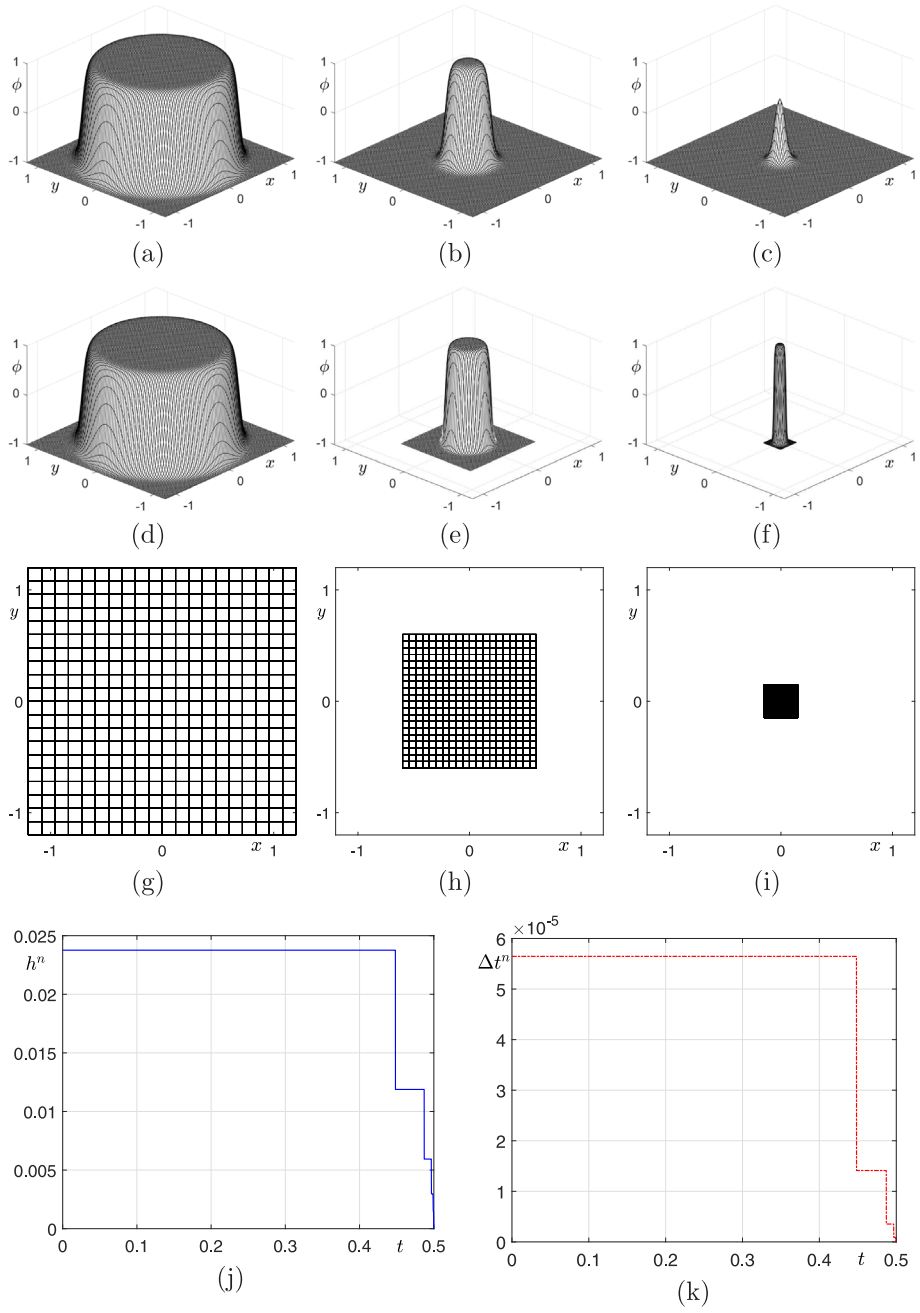

Fig. 3. Comparison of results for uniform mesh (first row, (a)–(c)) and adaptive refinement mesh with time-dependent interfacial parameter (second row, (d)–(f)). Temporal evolution of the adaptive meshes is shown, with each mesh represented only by 20% visibility for clarity (third row, (g)–(i)). The temporal evolutions of the phase-field function at times $t = 0$, 0.4574, and 0.4969 are shown from left to right. Transition of h^n is depicted in (j), and the transition of Δt^n is illustrated in (k).

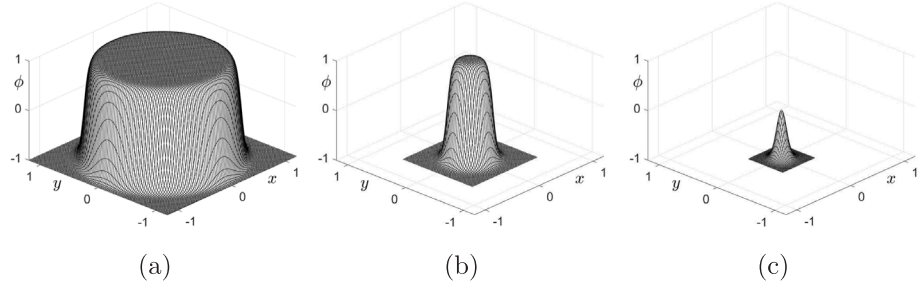

Fig. 4. Temporal evolution of the phase-field function for adaptive refinement mesh with constant interfacial parameter at times (a) $t = 0$, (b) 0.4574, and (c) 0.4969.

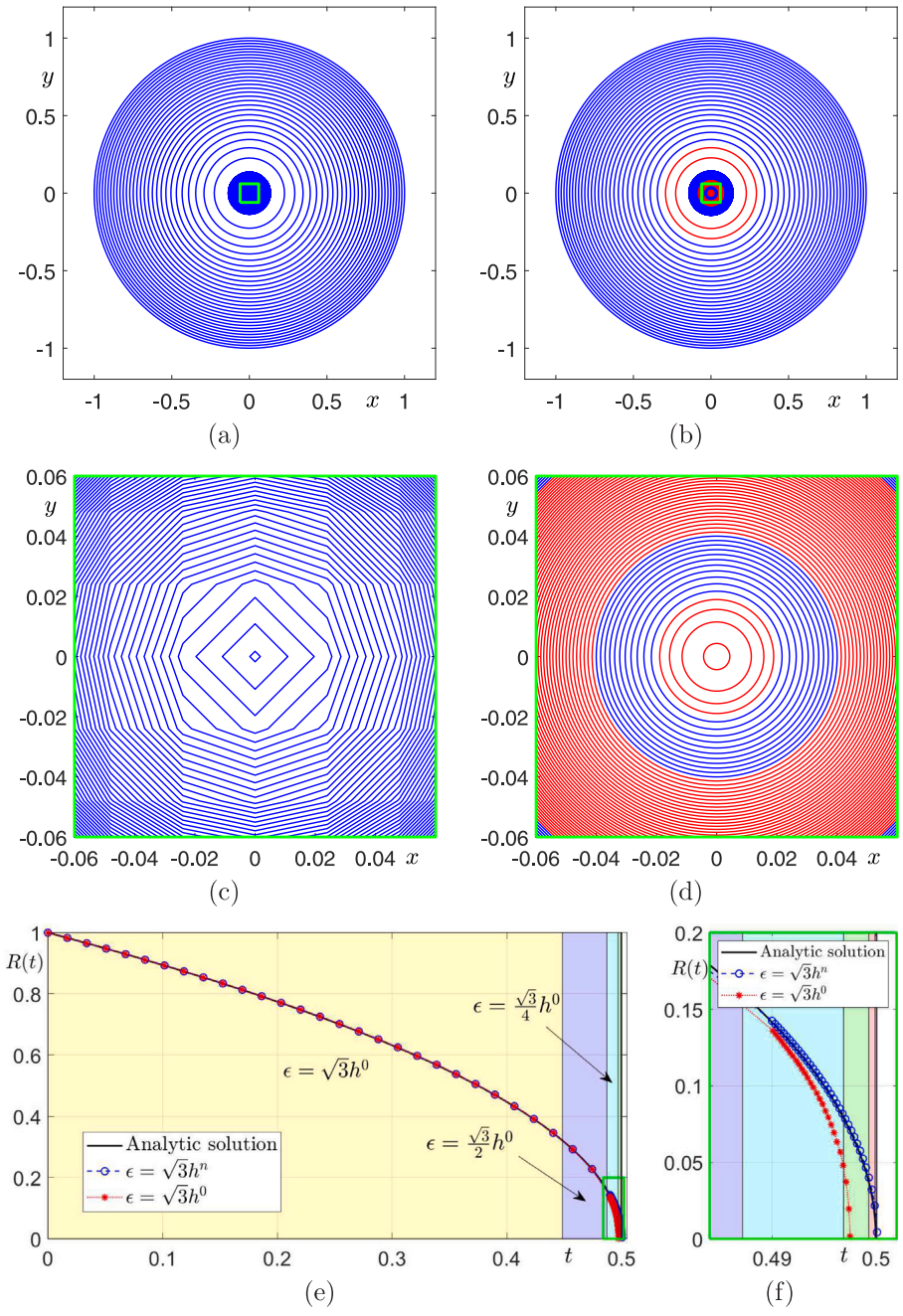

Fig. 5. (a) and (b) are the temporal evolution of the shrinking circle due to the motion by mean curvature with uniform mesh; and adaptive refinement mesh and parameter. (c) and (d) are enlarged figures of (a) and (b) within the boxed area. (e) is the temporal evolution of the radius of the shrinking circle due to the motion by mean curvature with the exact solution. (f) is a magnified view of (e) within the boxed area.

2.1. Numerical solution algorithm

Let $\Omega^0 = (L_x^0,\ R_x^0) \times (L_y^0,\ R_y^0)$ be the initial computational domain, and $\Omega_d^0 = \{(x_i,\ y_j)|x_i = L_x^0 + ih^0,\ y_j = L_y^0 + jh^0,\ i = 0, \dots, N_x^0$ and $j = 0, \dots, N_y^0\}$ be its discrete domain, where N_x^0 and N_y^0 are integers. Here, $h^0 = (R_x^0 - L_x^0)/N_x^0$ is the space step. Let $\phi_{ij}^n = \phi(x_i, y_j, t^n)$, where t^n is the time. Let $\Delta t^n = t^{n+1} - t^n$ be the adaptive time step at time $t = t^n$. Other adaptive time step methods are discussed in [22]. From now on, we use the superscript n for nth time variables: Ω^n, L_x^n, R_x^n, L_y^n, R_y^n, Ω_d^n, N_x^n, N_y^n, h^n, and Δt^n. Many numerical methods for the AC equation exist, such as the operator splitting method [23] and stable explicit method [24]. For simplicity of exposition, we use the explicit Euler scheme for the two-dimensional AC model with the time-dependent interfacial parameter:

$$\frac{\phi_{ij}^{n+1} - \phi_{ij}^n}{\Delta t^n} = -\frac{F'(\phi_{ij}^n)}{\epsilon^2(t^n)} + \Delta_d \phi_{ij}^n, \tag{3}$$

where $\Delta_d \phi_{ij}^n = [\phi_{i-1,j+1}^n + \phi_{i+1,j+1}^n + \phi_{i-1,j-1}^n + \phi_{i+1,j-1}^n + 4(\phi_{i-1,j}^n + \phi_{i+1,j}^n + \phi_{i,j-1}^n + \phi_{i,j+1}^n) - 20\phi_{ij}^n]/[6(h^n)^2]$ is the two-dimensional isotropic nine-point discretization for the Laplace operator. If we rewrite Eq. (3), then we obtain the following update scheme: For $i = 1, \dots, N_x^n - 1$ and $j = 1, \dots, N_y^n - 1$,

$$\phi_{ij}^{n+1} = \phi_{ij}^n + \Delta t^n \left(-\frac{F'(\phi_{ij}^n)}{\epsilon^2(t^n)} + \Delta_d \phi_{ij}^n \right), \tag{4}$$

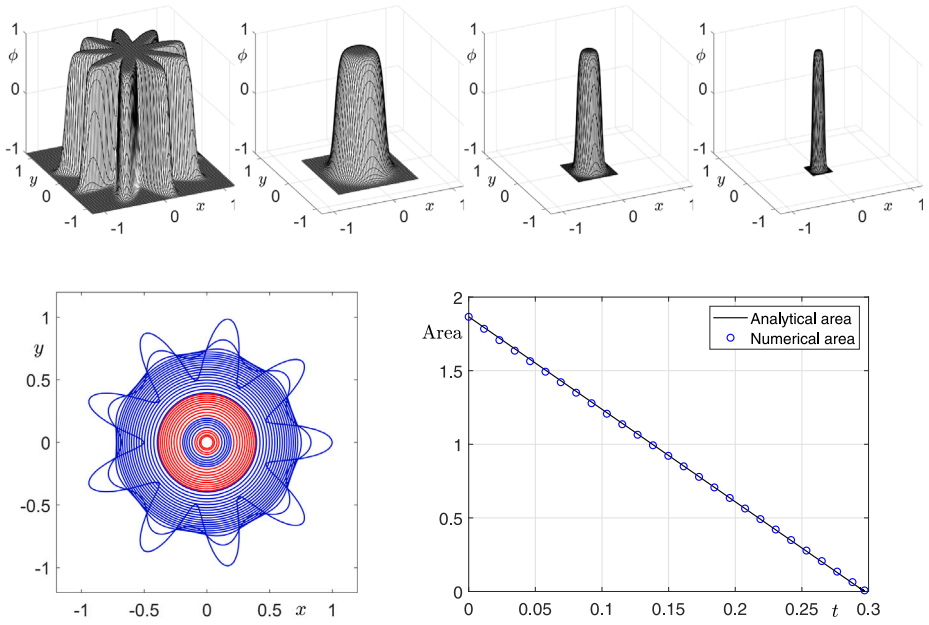

Fig. 6. (a)–(d) represent the temporal evolution of a star-shaped initial condition at $t = 0,\ 0.2230,\ 0.2794$, and 0.2935. (e) depicts the zero-level contour of the temporal evolution. (f) represents the change in area over time.

where we use the negative one Dirichlet boundary condition for simplicity. That is, $\phi^n_{i0} = -1,\ \phi^n_{iN^n_y} = -1$, for $i = 0, \dots, N^n_x$ and $\phi^n_{0j} = -1,\ \phi^n_{N^n_x j} = -1$, for $j = 0, \dots, N^n_y$.

It should be noted that the proposed AC model with a time-dependent parameter can be discretized with more stable and accurate numerical methods, as discussed in [25].

Curve shortening flow of any closed curve develops a singularity in finite time [17]. To numerically capture the evolution of the interface as it approaches singularity, we need infinitesimally small spatial and temporal steps. Furthermore, we need to reduce the interfacial transition parameter ϵ to zero simultaneously. Assuming the phase-field ϕ changes from -0.9 to 0.9 over the interfacial region with m space grid points, the ϵ value at time $t = t^n$ is defined by $\epsilon(t^n) = \epsilon_m(t^n) = h^n m/(2\sqrt{2}\tanh^{-1}(0.9))$, where h^n is the uniform mesh size at time $t = t^n$ [26].

The proposed numerical algorithm for investigating motion by mean curvature flow up to the singularity of curves is as follows: First, we solve the discrete AC equation (4) on the initial discrete domain Ω^0_d using the initial parameter values of ϕ^0, Δt^0, and $\epsilon = \epsilon(t^0)$. Second, during the temporal updating process, if ϕ^n satisfies some given conditions, then we adjust computational and model parameters by halving the space step and ϵ. For example, one of the criteria can be a change in the area enclosed by the zero-level contour of the order parameter. If the area is less than half of the area at the previous checkpoint time, then we will adjust the computational and model parameters. Fig. 2 shows a schematic illustration of the adaptive mesh refinement for discrete domains: (a) is Ω^p_d and ϕ^p, (b) is ϕ^q satisfying the adjustment criterion, (c) Ω^q_d and ϕ^q, and (d) Ω^r_d and ϕ^r. Here, $p < q < r$.

2.2. Numerical experiments

2.2.1. Circular initial condition

A circular initial condition on the domain $\Omega = (-1.2,\ 1.2) \times (-1.2,\ 1.2)$ is given as follows:

$$\phi(x, y, 0) = \tanh\left(\frac{1 - \sqrt{x^2 + y^2}}{\sqrt{2}\epsilon}\right). \tag{5}$$

Then, the zero-level contour of the phase-field ϕ corresponds to a circle γ. The radius $R(t)$ of γ evolves according to the following differential equation

$$\frac{dR(t)}{dt} = -\frac{1}{R(t)} \quad \text{with initial radius } R(0) = R_0 = 1. \tag{6}$$

The solution of Eq. (6) is given by $R(t) = \sqrt{R_0^2 - 2t}$. We know that $R(t) \to 0$ as $t \to R_0^2/2$. That is, the circle shrinks to a point in finite time and develops a singularity at a specific time $t = R_0^2/2$. The first row and the second row in Fig. 3 display the temporal evolutions of the phase-field function using uniform and adaptive refinement of both the grid and the parameter ϵ, respectively. In the third row of Fig. 3, the temporal evolution of the adaptive meshes is shown at 20% visibility for clarity. The times are $t = 0,\ 0.4574$, and 0.4969, from left to right columns. Fig. 3(j) and (k) show temporal evolutions of h^n and Δt^n, respectively. Note that we use an adaptive time-stepping technique to improve computational efficiency [27]. Fig. 4 displays the temporal evolution of the phase-field function for an adaptive refinement mesh with a constant interfacial parameter at times $t = 0,\ 0.4574$, and 0.4969. Here, we use $\epsilon(t) = \sqrt{3}h^0$ for the constant interfacial parameter and $\Delta t = 0.1(h^0)^2$ for the time step. From the results of Figs. 3 and 4, both the adaptive refinement mesh and the corresponding time-dependent interfacial parameter are necessary to resolve small-sized problems effectively.

Fig. 5(a) is the zero-level contour of the first row of Fig. 3, which is the result for a uniform mesh. Fig. 5(b) is the zero-level contour of the second row of Fig. 3, which is the result for an adaptive refinement mesh and parameter. Fig. 5(a) and (b) are plotted every $300\Delta t^0$. Fig. 5(c) and (d) are enlarged views of (a) and (b) in the boxed area, respectively. In Fig. 5, we can confirm that as time progresses, the uniform mesh solution does not have the shape of a circle due to insufficient grid resolution. Fig. 5(e) displays the evolutions of the radius of the shrinking circle due to the motion by mean curvature with the exact solution, the uniform mesh result, and the adaptive refinement mesh result, and (f) is a magnified view of (e) in the boxed area. Here, $N_x = N_y = 100$, $h^0 = 2.4/N_x$, $\Delta t^0 = 0.1(h^0)^2$, and $\epsilon^0 = \sqrt{3}h^0$

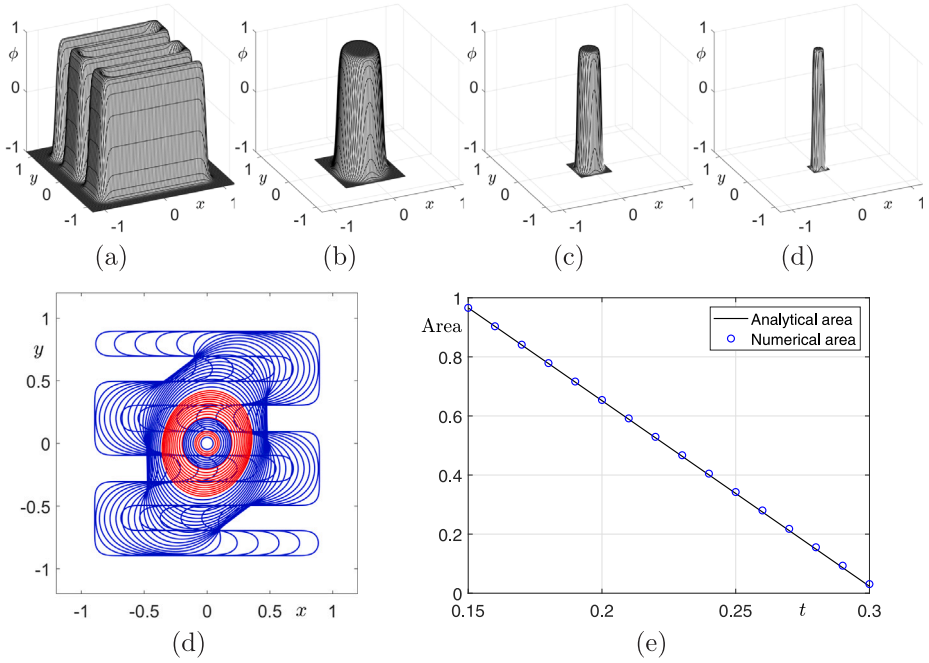

Fig. 7. (a)–(d) represent the temporal evolution of a winding-shaped initial condition at $t = 0,\ 0.2292,\ 0.2860$, and 0.3002. (e) depicts the zero-level contour of the temporal evolution. (f) represents the change in area over time.

are used. We can visually confirm that the computational solution is in an excellent agreement with the analytic solution $R(t) = \sqrt{1-2t}$ until the singular time $t = 0.5$. However, as shown in the magnified view, Fig. 5(f), the numerical solution deviates from the exact solution. The calculated value of ϵ used as the minimum value is 7.31106606e−17.

2.2.2. Complex initial conditions

Numerical experiments are conducted not only on symmetric circular initial conditions but also on complex initial conditions. First, we consider the evolution over time of the star-shaped initial condition:

$$\phi(x, y, 0) = \tanh\left(\frac{0.75 + 0.25\cos 9\theta - \sqrt{x^2+y^2}}{\sqrt{2}\epsilon}\right),$$

where θ is the angle between the line passing through the origin and the point (x, y) and the x-axis. Here are the parameters used on $\Omega^0 = (-1.2,\ 1.2)\times(-1.2,\ 1.2)$: $N_x^0 = N_y^0 = 100$, $\epsilon(0) = 2h$, $\Delta t = 0.1h^2$. Fig. 6(a)–(d) capture the phase of ϕ each time the mesh is refined. Fig. 6(e) shows the zero-level contour of ϕ over time. Fig. 6(f) compares the area of ϕ with the analytically computed area, which indicates that the area enclosed by a simple closed curve decreases by 2π [28]. The numerical area of ϕ is calculated from the zero-level contour of ϕ.

Furthermore, we consider a winding-shaped initial condition on $\Omega^0 = (-1.2,\ 1.2)\times(-1.2,\ 1.2)$. The parameters used here are $N_x^0 = N_y^0 = 240$, $\epsilon(0) = \sqrt{7}h$, and $\Delta t = 0.2h^2$. Fig. 7(a) is a winding-shaped initial condition. Fig. 7(b)–(d) show the phase of ϕ at $t = 0,\ 0.2292,\ 0.2860$, and 0.3002 which correspond to the times when the mesh is refined. Fig. 7(e) is the temporal evolution as represented by the zero-level contour of ϕ. We can observe the change in the area matches well with the theoretical prediction.

Next, we numerically justify that the proposed scheme for the time-dependent interfacial transition parameter is optimal. As shown in Fig. 8, when the spatial step is halved at $n = N_l$ with $l = 1, 2, \dots$, the time-dependent interface parameter $\epsilon(t)$ decreases. It is noted that $N_0 = 0$. Let us define the time-dependent interfacial transition parameter as $\epsilon^n = (\sqrt{3}h^0)/a^l$ for $N_l \le n < N_{l+1}$. Fig. 9 shows temporal evolutions

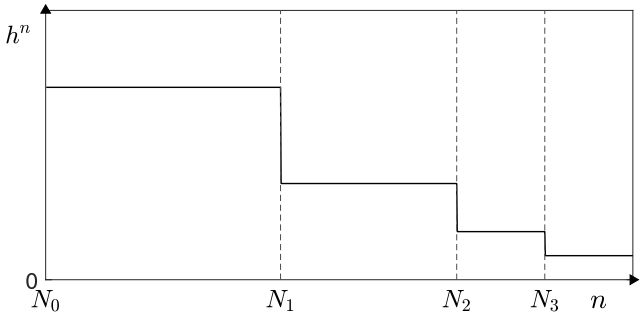

Fig. 8. Schematic illustration for the temporal evolution of h^n at $t = N_1,\ N_2$, and N_3.

of the numerical solutions for various time-dependent interfacial parameters with $a = 1.5$, $a = 2$, and $a = 3.3$. In Fig. 9, we consider the circular initial condition in Eq. (6) on a computational domain $(-1.2, 1.2)\times(-1.2, 1.2)$. Here, we use $N_x^0 = N_y^0 = 100$ and $\epsilon^0 = \sqrt{3}h^0$. In the result shown in Fig. 9(a), the interfacial thickness increases and becomes too diffusive relative to the space step size as time evolves. In Fig. 9(c), the solution is pinned and does not evolve due to the relatively small value of ϵ as we refine the space step. In the case of Fig. 9(b), the solution maintains a constant interfacial thickness as the space step decreases in size. Therefore, we can justify that the time-dependent interfacial parameter is optimal with $a = 2$.

3. Three-dimensional space

Next, we present a computational algorithm and perform numerical experiments for the 3D AC equation with a time-dependent parameter for motion by mean curvature up to the singularity.

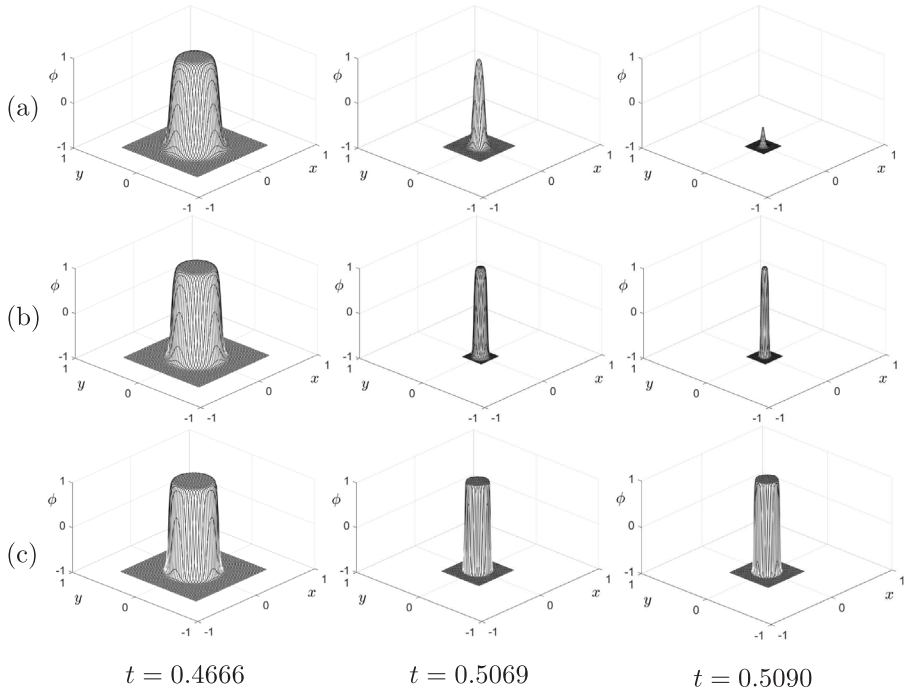

Fig. 9. Temporal evolutions of the numerical solutions for various time-dependent interfacial parameters with (a) $a = 1.5$, (b) $a = 2$, and (c) $a = 3.3$.

3.1. Numerical solution algorithm

Let $\Omega^0 = (L_x^0,\ R_x^0)\times(L_y^0,\ R_y^0)\times(L_z^0,\ R_z^0)$ be the initial computational domain and $\Omega_d^0 = \{(x_i,\ y_j,\ z_k)|x_i = L_x^0 + ih^0,\ y_j = L_y^0 + jh^0,\ z_k = L_z^0 + kh^0,\ i = 0,\dots,N_x^0,\ j = 0,\dots,N_y^0,$ and $k = 0,\dots,N_z^0\}$ be its discrete domain, where N_x^0, N_y^0, N_z^0 are integers. Here, $h^0 = (R_x^0 - L_x^0)/N_x^0$ is the space step. Let $\phi_{ijk}^n = \phi(x_i, y_j, z_k, t^n)$. From now on, we use the superscript n for nth time variables: Ω^n, L_x^n, R_x^n, L_y^n, R_y^n, L_z^n, R_z^n, Ω_d^n, N_x^n, N_y^n, N_z^n, h^n, and Δt^n. For simplicity of exposition, let us use the explicit Euler method for the three-dimensional AC model with the time-dependent interfacial parameter:

$$\frac{\phi_{ijk}^{n+1} - \phi_{ijk}^n}{\Delta t^n} = -\frac{F'(\phi_{ijk}^n)}{\epsilon^2(t^n)} + \Delta_d \phi_{ijk}^n, \tag{7}$$

where $\Delta_d \phi_{ijk}^n = \big[\ 20(\phi_{i+1,jk}^n + \phi_{i-1,jk}^n + \phi_{i,j-1,k}^n + \phi_{ij,k-1}^n + \phi_{i,j+1,k}^n + \phi_{ij,k+1}^n) + 6(\phi_{i-1,j+1,k}^n + \phi_{i-1,j-1,k}^n + \phi_{i+1,j+1,k}^n \phi_{i+1,j-1,k}^n + +\phi_{i,j-1,k+1}^n + \phi_{i,j-1,k-1}^n + \phi_{i,j+1,k+1}^n + \phi_{i,j+1,k-1}^n + \phi_{i-1,j,k+1}^n + \phi_{i-1,j,k-1}^n + \phi_{i+1,j,k+1}^n + \phi_{i+1,j,k-1}^n) + \phi_{i-1,j-1,k-1}^n + \phi_{i-1,j+1,k-1}^n + \phi_{i-1,j-1,k+1}^n + \phi_{i+1,j-1,k-1}^n + \phi_{i-1,j+1,k+1}^n + \phi_{i+1,j+1,k-1}^n + \phi_{i+1,j+1,k+1}^n + \phi_{i+1,j-1,k+1}^n - 200\phi_{ijk}^n\ \big]/(48(h^n)^2)$ is a three-dimensional isotropic 27-point discretization for the Laplace operator [29]. If we rewrite Eq. (7), then we have the following update method: For $i = 1,\dots,N_x - 1,\ j = 1,\dots,N_y - 1,$ and $k = 1,\dots,N_z - 1,$

$$\phi_{ijk}^{n+1} = \phi_{ijk}^n + \Delta t^n \left(-\frac{F'(\phi_{ijk}^n)}{\epsilon^2(t^n)} + \Delta_d \phi_{ijk}^n \right), \tag{8}$$

where we use the negative one Dirichlet boundary condition.

3.2. Numerical experiments

A spherical initial profile on a domain $\Omega = (-1.2,\ 1.2)\times(-1.2,\ 1.2)\times(-1.2,\ 1.2)$ is given as follows:

$$\phi(x, y, z, 0) = \tanh\left(\frac{1 - \sqrt{x^2 + y^2 + z^2}}{\sqrt{2}\epsilon} \right). \tag{9}$$

Here, $N_x = N_y = N_z = 100$, $h = 2.4/N_x$, and $\Delta t = 0.1h^2$ are used. The zero-level isosurface of the phase-field ϕ represents a spherical surface γ. The radius $R(t)$ of γ evolves according to the differential equation

$$\frac{dR(t)}{dt} = -\frac{2}{R(t)} \quad \text{with initial radius } R(0) = R_0 = 1. \tag{10}$$

The analytic solution of Eq. (10) is given by $R(t) = \sqrt{R_0^2 - 4t}$. We know that $R(t) \to 0$ as $t \to R_0^2/4$. That is, the spherical surface shrinks to a point in finite time and develops a singularity at time $t = R_0^2/4$. Numerical parameters $N_x = N_y = 100$, $h^0 = 2.4/100$, $\Delta t^0 = 0.1(h^0)^2$, and $\epsilon^0 = \sqrt{3}h^0$ are used for the following numerical experiments.

Fig. 10(a)–(c) display the evolution of the zero-level isosurface of the phase field and the adaptive refinement domain at times $t = 0$, 0.2397, and 0.2514, from left to right, respectively. In Fig. 10(d)–(f), the temporal evolution of the 3D adaptive meshes is represented with each mesh shown at only 10% visibility for clarity. Fig. 10(g) and (h) show the temporal transition of h^n and Δt^n, respectively.

Fig. 11(a) and (b) are snapshots of the zero-level isosurface of phase-field functions at $t = 0.2431$, $t = 0.2463$, and $= 0.2490$ with uniform and adaptive refinement mesh, respectively. Fig. 5(c) shows the evolutions of the radii of the shrinking circle as a result of the motion by mean curvature. The results of the analytic solution, uniform mesh, and adaptive refinement mesh are shown. The numerical results of both uniform mesh and adaptive refinement mesh agree with the analytic solution $R(t) = \sqrt{1 - 4t}$ before the radius is less than about $R = 0.2$. However, as shown in the magnified view, Fig. 11(d), the numerical result of the uniform mesh deviates from the analytic solution. We can observe that the result of the adaptive refinement shows good agreement with the analytic solution until just before time $t = 0.25$. The minimum value of the calculated time-dependent interfacial parameter $\epsilon(t^n)$ is 7.31106606e−17.

Next, we consider complex initial conditions in 3D space. On a computational domain $(-1, 1)\times(-1, 1)\times(-1, 1)$, we consider the following initial condition: a sphere with the center at the origin and radius 0.7,

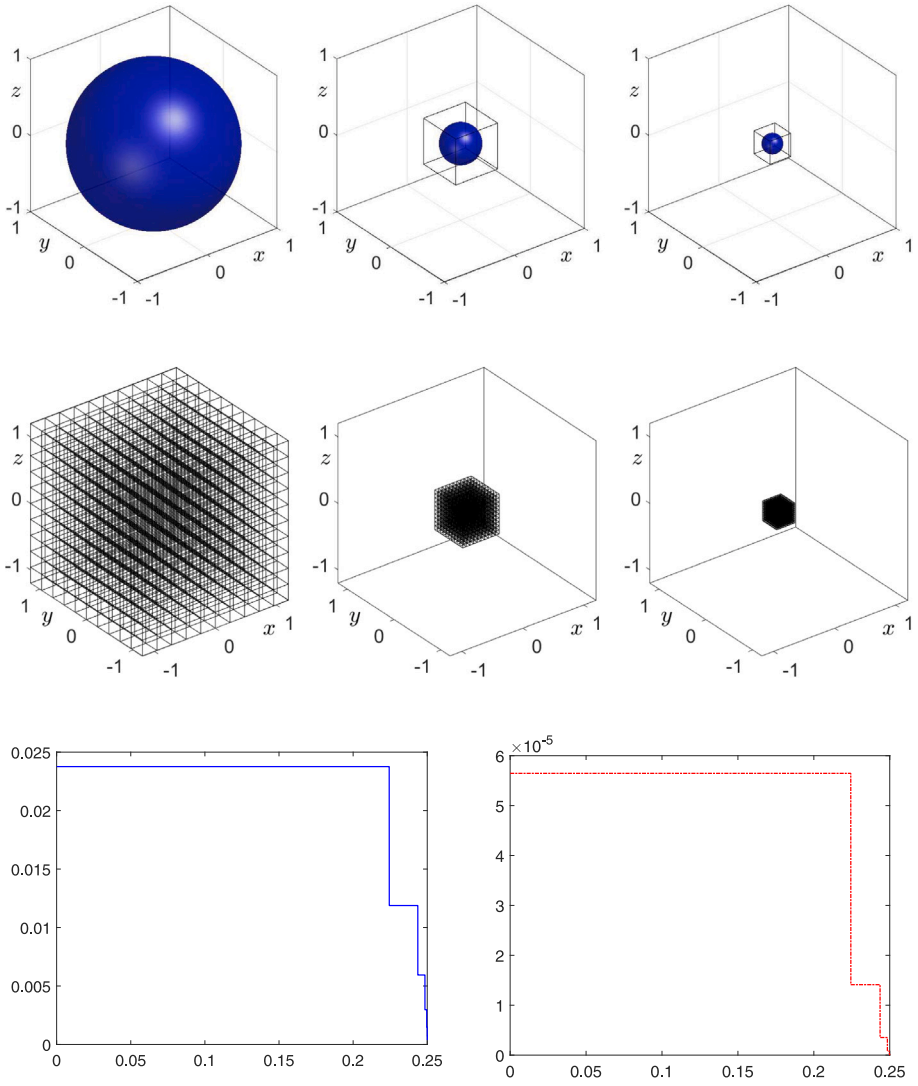

Fig. 10. (a)–(c) Evolution of the zero-level isosurface of the phase-field function and adaptive mesh refinement discrete domain. (d)–(f) Temporal evolution of the 3D adaptive mesh is displayed, with each mesh represented at only 10% visibility for clarity. The temporal evolutions of the first and second row are shown at times $t = 0$, $t = 0.2397$, and $t = 0.2514$. Temporal transition of (g) h^n and (h) Δt.

perturbed by a spherical harmonic $Y_{l,m}$ [30].

$$\phi(x, y, z, 0) = \tanh\left(\frac{0.7 - \sqrt{x^2 + y^2 + z^2} + 0.7Y_{l,m}(\theta, \varphi)}{\sqrt{2}\epsilon^0}\right),$$

where θ is the polar angle and φ is the azimuthal angle. Here, we use $N_x^0 = 99$, $\epsilon(0) = \sqrt{3}h^0$, and $\Delta t^0 = 0.1(h^0)^2$. Fig. 12 shows the snapshots at $t = 0$, $t = 0.0846$, $t = 0.1128$, and $t = 0.1208$.

We consider winding-shaped initial condition as shown in Fig. 13(a) with parameters $N_x^0 = N_y^0 = N_z^0 = 99$, $\epsilon^0 = \sqrt{3}h^0$, and $\Delta t^0 = 0.1(h^0)^2$ on $(-1, 1) \times (-1, 1) \times (-1, 1)$. Fig. 13 displays the temporal evolution of the zero-level isosurface of the computational solutions. The results for the complex initial conditions indicate that the temporal evolution follows the motion by mean curvature.

4. Conclusions

In this article, we presented the novel AC model with a time-dependent interfacial thickness parameter to study the temporal evolution of 2D and 3D interfaces under motion driven by mean curvature up to singularities. To show the high performance of the proposed mathematical equation and its computational algorithm, we presented various numerical experiments and studied motion by mean curvature up to the singularities of curves and interfaces. The numerical experiments validated the superior performance of the proposed model and its numerical method. The proposed time-dependent parameter methodology and its adaptive mesh scheme can be successfully applied to other similar mathematical models [31] and curved surfaces [32] for investigating singularities. Furthermore, the proposed novel AC model can be used as a benchmark for solving partial differential equations with changing model parameters using adaptive physics informed neural networks [33]. There is interesting future work in extending the proposed methodology to the multidimensional AC equation [34,35]. In this study, we focused on presenting a novel AC model with a time-dependent interfacial thickness parameter and its numerical method. We numerically validate that this time-dependent parameter enables the corresponding limiting motion to coincide with the motion by mean curvature. As another future research direction, it would be valuable to theoretically prove the numerical findings, such as the motion by mean curvature of the modified AC equation with a time-dependent interfacial parameter.

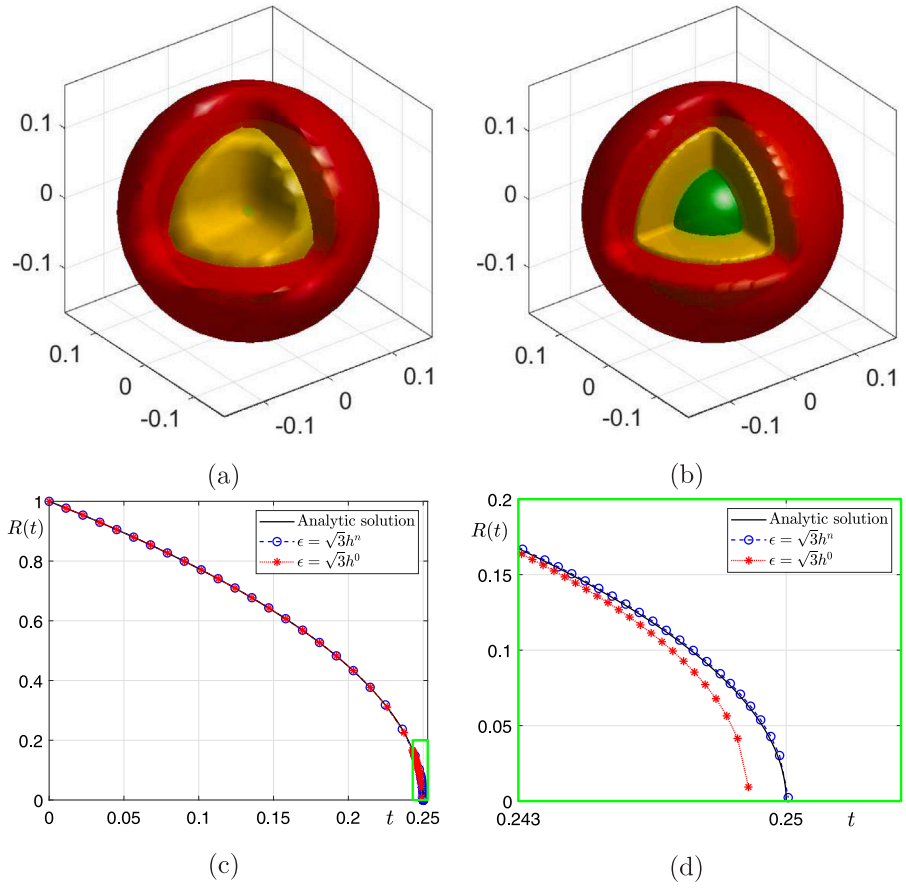

Fig. 11. (a) and (b) Evolutions of zero-level isosurface of phase-field function at times $t = 0.2431$, $t = 0.2463$, and $t = 0.2490$ with uniform and adaptive refinement mesh. (c) Temporal evolution of the radii of the shrinking sphere due to motion by mean curvature with the exact solution. (d) Magnified view of (c) in the boxed area.

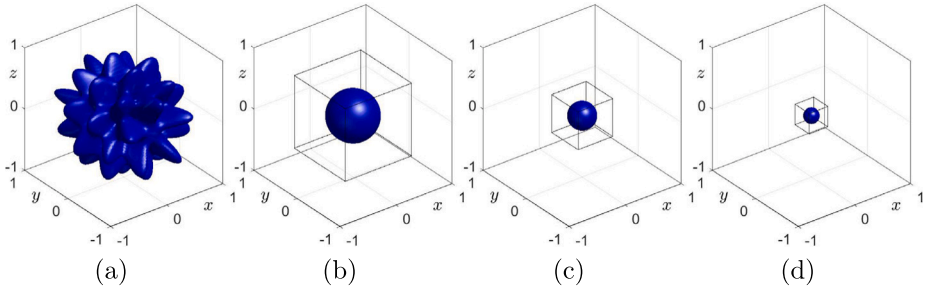

Fig. 12. In 3D space, the temporal evolution of a perturbed spherical harmonic initial condition at (a) $t = 0$, (b) $t = 0.0846$, (c) $t = 0.1128$, and (d) $t = 0.1208$.

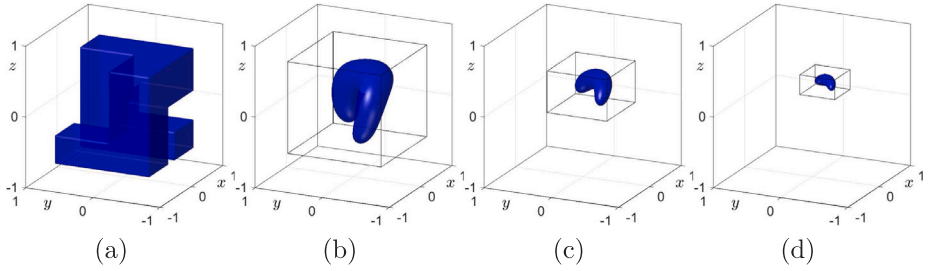

Fig. 13. In 3D space, the temporal evolution of a winding-shaped initial condition at (a) $t = 0$, (b) $t = 0.0564$, (c) $t = 0.0761$, and (d) $t = 0.082$.

CRediT authorship contribution statement

Junxiang Yang: Writing – review & editing, Writing – original draft, Validation, Methodology, Formal analysis, Conceptualization. **Dongsun Lee:** Methodology, Investigation, Formal analysis, Conceptualization. **Soobin Kwak:** Writing – review & editing, Writing – original draft, Visualization, Software, Investigation. **Seokjun Ham:** Writing – review & editing, Writing – original draft, Visualization, Software, Formal analysis. **Junseok Kim:** Writing – review & editing, Writing – original draft, Supervision, Resources, Methodology, Formal analysis, Conceptualization.

Declaration of competing interest

The authors declare that they have no known competing financial interests or personal relationships that could have appeared to influence the work reported in this paper.

Data availability

No data was used for the research described in the article.

Acknowledgments

J. Yang is supported by Macau University of Science and Technology Faculty Research Grants (FRG) (No. FRG-24-026-FIE). D. Lee was supported by the National Research Foundation of Korea (NRF-2018R1D1A1B07049292). The corresponding author (J.S. Kim) was supported by the National Research Foundation of Korea (NRF) grant funded by the Korea government (MSIT) (No. 2022R1A2C1003844). The authors express their gratitude to the reviewers for their valuable comments during the revision process of this article.

References

[1] Fattebert JL, DeWitt S, Perron A, Turner J. Thermo4PFM: Facilitating phase-field simulations of alloys with thermodynamic driving forces. Comput Phys Commun 2023;288:108739.
[2] Li Y, Lan S, Liu X, Lu B, Wang L. An efficient volume repairing method by using a modified Allen–Cahn equation. Pattern Recogn 2020;107:107478.
[3] Kim Y, Ryu G, Choi Y. Fast and accurate numerical solution of Allen–Cahn equation. Math Probl Eng 2021;2021:1–12.
[4] Kim Y, Lee D. Numerical investigation into the dependence of the Allen–Cahn equation on the free energy. Adv Comput Math 2022;48(3):1–32.
[5] Aguilera-Rojas PJ, Alfaro-Bittner K, Clerc MG, González-Cortés G, Rojas RG. The universal law of the front speed close to the disappearance of bistability. Chaos Solitons Fractals 2023;169:113241.
[6] Tan Z, Zhang C. The discrete maximum principle and energy stability of a new second-order difference scheme for Allen–Cahn equations. Appl Numer Math 2021;166:227–37.
[7] Deng D, Zhao Z. Efficiently energy-dissipation-preserving ADI methods for solving two-dimensional nonlinear Allen–Cahn equation. Comput Math Appl 2022;128:249–72.
[8] Wang J, Han Z, Jiang W, Kim J. A fast, efficient, and explicit phase-field model for 3D mesh denoising. Appl Math Comput 2023;458:128239.
[9] Lee S, Yoon S, Lee C, Kim S, Kim H, Yang J, Kwak S, Hwang Y, Kim J. Effective time step analysis for the Allen–Cahn equation with a high-order polynomial free energy. Int J Numer Methods Eng 2022;123:4726–43.
[10] Lee HG. High-order and mass conservative methods for the conservative Allen–Cahn equation. Comput Math Appl 2016;72(3):620–31.
[11] Li Y, Xia Q, Yoon S, Lee C, Lu B, Kim J. Simple and efficient volume merging method for triply periodic minimal structures. Comput Phys Commun 2021;264:107956.
[12] Owolabi KM, Jain S. Spatial patterns through diffusion-driven instability in modified predator–prey models with chaotic behaviors. Chaos Solitons Fractals 2023;174:113839.
[13] Lan R, Li J, Cai Y, Ju L. Operator splitting based structure-preserving numerical schemes for the mass-conserving convective Allen–Cahn equation. J Comput Phys 2023;472:111695.
[14] Li H, Song Z, Hu J. Numerical analysis of a second-order IPDGFE method for the Allen–Cahn equation and the curvature-driven geometric flow. Comput Math Appl 2021;86:49–62.
[15] Li C, Huang Y, Yi N. An unconditionally energy stable second order finite element method for solving the Allen–Cahn equation. J Comput Appl Math 2019;353:38–48.
[16] Chen Y, Huang Y, Yi N. A SCR-based error estimation and adaptive finite element method for the Allen–Cahn equation. Comput Math Appl 2019;78(1):204–23.
[17] Chen J, He W. A note on singular time of mean curvature flow. Math Z 2010;266:921–31.
[18] Bertozzi A, Esedoglu S, Gillette A. Analysis of a two-scale Cahn–Hilliard model for binary image inpainting. Multiscale Model Simul 2007;6(3):913–36.
[19] Ferrer E, Rubio G, Ntoukas G, Laskowski W, Mariño OA, Colombo S, Mateo-Gabín A, Marbona H, Manrique de Lara F, Huergo D, Manzanero J, Rueda-Ramírez AM, Kopriva DA, Valero E. A high-order discontinuous Galerkin solver for flow simulations and multi-physics applications. Comput Phys Commun 2023;287:108700.
[20] Jeong DR, Li Y, Lee HG, Kim JS. Fast and automatic inpainting of binary images using a phase-field model. J Korean Soc Ind Appl Math 2009;13(3):225–36.
[21] Yang J, Kim J. Computer simulation of the nonhomogeneous zebra pattern formation using a mathematical model with space-dependent parameters. Chaos Solitons Fractals 2023;169:113249.
[22] Lee C, Park J, Kwak S, Kim S, Choi Y, Ham S, Kim J. An adaptive time-stepping algorithm for the Allen–Cahn equation. J Funct space 2022;2022.
[23] Park J, Lee C, Choi Y, Lee HG, Kwak S, Hwang Y, Kim J. An unconditionally stable splitting method for the Allen–Cahn equation with logarithmic free energy. J Eng Math 2022;132(1):18.
[24] Lee C, Choi Y, Kim J. An explicit stable finite difference method for the Allen–Cahn equation. Appl Numer Math 2022;182:87–99.
[25] Uzunca M, Karasözen B. Linearly implicit methods for Allen–Cahn equation. Appl Math Comput 2023;450:127984.
[26] Li Y, Lee HG, Jeong D, Kim J. An unconditionally stable hybrid numerical method for solving the Allen–Cahn equation. Comput Math Appl 2010;60(6):1591–606.
[27] Huang S, Xiao X, Feng X. An adaptive time-stepping method for the phase-field molecular beam epitaxial growth model on evolving surfaces. Appl Math Comput 2023;439:127622.
[28] Gage M, Hamilton RS. The heat equation shrinking convex plane curves. J Differ Geom 1986;23(1):69–96.
[29] Yoon S, Lee HG, Li Y, Lee C, Park J, Kim S, Kim H, Kim J. Benchmark problems for the numerical discretization of the Cahn–Hilliard equation with a source term. Discrete Dyn Nat Soc 2021;2021:1–11.
[30] Wieczorek MA, Meschede M. Shtools: Tools for working with spherical harmonics. Geochem Geophys Geosy 2018;19(8):2574–92.
[31] Lee D, Lee C. Numerical solutions of the Allen–Cahn equation with the p-Laplacian. Appl Math Comput 2022;434:127435.
[32] Chen M, Ham S, Choi Y, Kim H, Kim J. Pattern dynamics of a harvested predator–prey model. Chaos Solitons Fractals 2023;176:114153.
[33] Zhao CL. Solving Allen–Cahn and Cahn–Hilliard equations using the adaptive physics informed neural networks. Commun Comput Phys 2021;29(3):930–54.
[34] Prakash A, Kaur H. Analysis and numerical simulation of fractional order Cahn–Allen model with Atangana–Baleanu derivative. Chaos Solitons Fractals 2019;124:134–42.
[35] Fang X, Qiao L, Zhang F, Sun F. Explore deep network for a class of fractional partial differential equations. Chaos Solitons Fractals 2023;172:113528.